FLOMEKO 2003
11th IMEKO TC9 Conference on Flow Measurement
Groningen, NETHERLANDS, 12 - 14 May 2003

NUMERICAL SIMULATION OF UNSTEADY THREE-DIMENSIONAL FLOW FIELDS IN A TURBINE FLOW METER

E. von Lavante, N. Lazaroski, U. Maatje, University of Essen, Essen, Germany
T. Kettner, V. Lötz-Dauer, Elster Production GmbH, Mainz-Kastell, Germany

Abstract

The complex three-dimensional unsteady flow field in a one-stage turbine gas flow meter was studied by carrying out numerical simulations using the Navier-Stokes solver Fluent. The simulation of all the viscous effects as well as secondary flows, such as the flow in the tip gap and secondary and tertiary vortices in the blade to blade region required a very high grid resolution. Therefore, a series of three-dimensional block-oriented hybrid grids containing between 300 thousand and 1.5 million grid cells was generated and implemented. The aim of the present project was to find the correct operating conditions to subsequently explain the behavior of the mechanical accuracy of the meter, to prove the correctness of the theory of operation and to verify these results by comparison with experimental measurements.

Introduction

Due to the circumstances given by today's growing energy consumption throughout the world and the opening of gas markets, the transportation and measurement of natural gas becomes more and more important. From an economical point of view of the customer and the vendor, the volume of sales of the gas has to be measured as accurately as possible. With respect to that, the requirements imposed on the measuring systems are very high. One flow meter that fulfills all the given requirements and is capable of measuring very accurately even under high pressures in field use is the turbine flow meter.

In the past, most of the investigations of turbine flow meters were done analytically and experimentally. Several authors focused on the development of an equation of motion of the meter by relating the driving torques of the fluid to the friction torques due to friction of the fluid on the hub, in the tip gap or in the bearing [1, 11, 13]. Many investigations [2, 7, 13, 14] studied the effect of pulsations or profile deformations on the accuracy of the meter. In the last two decades the self-correcting and self-proving gas turbine meters have been subject of intensive research. One working principle is based on the coupling of two rotors. A sensor rotor small distance downstream from the main rotor senses and responds to changes in the exit angle of the fluid leaving the main rotor [4, 9, 10, 11, 12]. Another working principle assumes two decoupled rotors in a two-stage turbine meter, where the second, the so-called reference rotor, works independently of the first one. The resulting two-stage turbine meter AccuTest^{TM} has been developed and investigated in recent years experimentally and analytically by Schieber [16, 17].

In recent work the flow in a two-stage meter was investigated numerically by the present authors [5, 8] using a two-dimensional cascade model consisting of both stages in order to reduce the computational time of the unsteady simulations. A DFT analysis of the unsteady behavior of the blade forces [8] confirmed the experimentally determined trends. Strong stator/rotor interactions, yielding a high variation of the unsteady blade forces in the second rotor were found, leading to modifications in the basic turbine flow meter design.

The main goal of the present work was to provide a detailed analysis of the three-dimensional unsteady flow field in the meter, hoping to get informations that would make it possible to explain the so-called high pressure shift of the mechanical accuraccy. Typically, this occurs in turbine meters when the operating pressure changes from $1\,bar$ to a higher pressure, mostly greater than $4\,bar$. To this end, the three-dimensional flow field, especially in the first stage ot the meter, was studied in detail. The aim was to identify possible sources of unfavourable flow effects in the meter. In all present computations the measured medium was assumed to be air at atmospheric conditions, making comparison with experimental data possible.

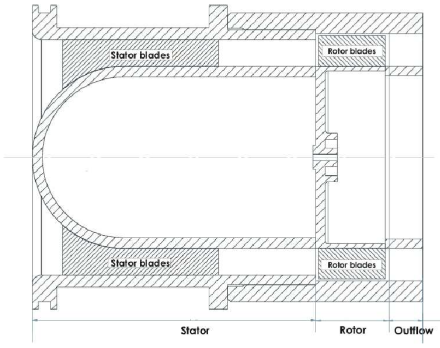

Figure 1: Cutaway drawing of the Elster TRZ DN80 turbine flow meter

Choice of Numerical Tools

Figure 1 shows a cutaway drawing of the turbine flow meter TRZ DN 80, manufactured by the Elster GmbH, that has been investigated in the present work. In order to make the flow simulation feasible, a few simplifying assumptions had to be made. In the original meter, there were 17 blades in the stator (flow conditioner) and 10 in the rotor. This design minimizes the danger of resonance, but requires the simulation of the entire meter, since the flow is periodic with respect to 2π. The present authors therefore assumed 20 blades in the stator and 10 blades in the rotor, employing the so called Reduced Blade Count approach. The flow field could now be treated as periodic in a segment consisting of 2 stator blades and one rotor blade. An isometric view of the entire configuration is offered in Fig. 2a, with the corresponding computational domain displayed in Fig. 2b. The geometry of the paticular meter simulated here was kept as original as possible, including all irregularities such as steps, dents, gaps and grooves, since these could affect the flow and, therefore, the accuracy as well.

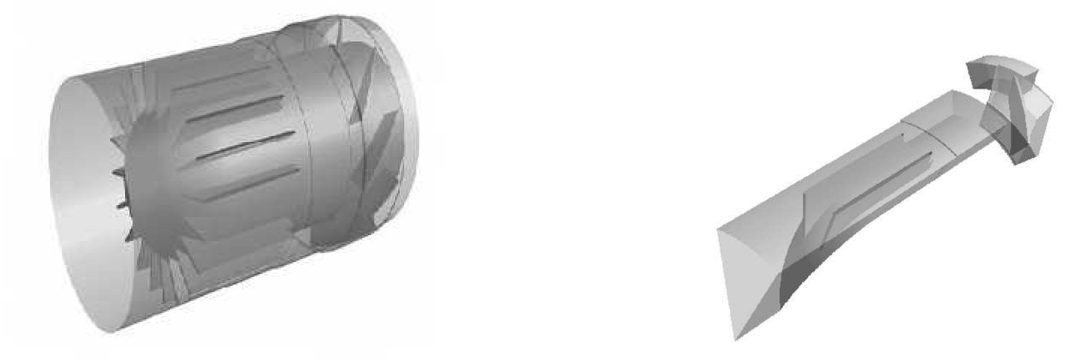

Figure 2: Isometric view of the entire geometry simulated (left) and the corresponding periodic segment (right)

The computational grid generation was accomplished using the GRIDGEN program, since it allowed the combination of structured and unstructured grids to be combined while being relatively easy to use (for more details, see the next section).

The flow solver selected for the present work was the Fluent system in version 6.x. Out of the many options available in this code, following combination was chosen:

- Accuracy in space was maintained at 2nd order for all the governing equations.
- Discretization in space was using the segregated scheme, since the flow was entering the meter at a maximum Mach number of Ma=0.04. It was, therefore, reasonable to assume that no nonlinearities existed in the flow field.
- The discretization in time was also 2nd order using an implicit subiteration in pseudotime. 20 iterations were judged sufficient.
- The working medium (air) was assumed to be an ideal compressible gas.
- The k-ϵ realizable turbulence model was used, employing wall functions where applicable. On the finer grids, no wall functions where necessary, since the resolution at the wall was better than $y^+ = 1$.

The flow was assumed to be compressible since locally (at sharp edges, for example) the flow could expand to Mach numbers higher than Ma = 0.3. Only the truly unsteady mode of computation was considered, with an time accurate stator-rotor interface implemented. Nonreflecting boundary conditions had to be used throughout the computational domain. The computations were carried out on a cluster of PC-type workstations using the Linux OS. The cluster is connected by a high performance network, making a moderately parallelized computations possible.

Inflow conditions
The flow meter selected for the present investigation had an annular inlet of D = 0.0775 m diameter. It was rated for maximum volumetric flow of $\dot{V} = 250m^3/h$. In the present simulations, two cases were considered: maximum volumetric flow Q_{max} and a much smaller volume flow rate $Q = 0.1 \cdot Q_{max}$. In the case of Q_{max}, the mean inflow velocity was $u_{in} = 14.72m/s$, the static pressure was $p = 1.01325 \cdot 10^5 Pa$ and the static temperatur T = 293.15 K. The corresponding Mach number was Ma = 0.04288 and the Reynolds number was $Re = 76 \cdot 10^3$. In the case of the smaller volume flow rate, the mean inflow velocity was $u_{in} = 1.472m/s$, while the static conditions remained the same. The other flow variables were changed accordingly.

The incoming velocity profile was assumed to be symmetric fully developed turbulent flow according to Nikuradse. The profile was obtained by carrying out numerical simulation of a corresponding pipe flow in two dimensions. The incoming turbulence level was set to 5 percent. Pressure inlet and outlet conditions were used to yield the desired mass flow rates. This procedure required adjusting the outlet pressure to a proper preset value in several iteration steps, and was therefore very time consuming.

Computational grid
As pointed out in previously, the emphasis of the present work was put on detailed analysis of the corresponding flow fields. Therefore, a two-dimensional configuration was judged insufficient due to its lack of any secondary and three-dimensional effects. On the other hand, severe restrictions were imposed due to the limited computational resources. The local RAM requirement had to be kept below 3.5 GB and the computational times should amount to less than a month. On the other hand, the establishment of the correct mass flow and the optimization of the operating conditions (see next chapter) required several computations for each volume flow case. In view of these problems, early in the present study a moderate grid refinement was carried out. Three computational grids with different resolution were compared:

- coarse grid, having approximately $350 \cdot 10^3$ grid cells
- medium grid with $1 \cdot 10^6$ grid cells
- very fine grid containing $1.5 \cdot 10^6$ grid cells

All the grids consisted of several blocks; over 98 % of the grids were structured using hexahedrals as cells. In the wake region behind the stator, an unstructured grid made of tetrahedrals was used due to the complex shape of the walls.

The coarse grid allowed quick unsteady computations, was able to capture all relevant global properties of the flow field, but was not adequate to resolve details of the structure of the shear layers. It was used to determine the operating conditions by minimizing the sum of all moments about the rotational axis. The very fine grid was very slow to converge and would just barely fit into the available RAM. Its use was not practical. The intermmediate grid possessed the proper resolution and was still small enough to be of practical use. It was judged by the authors as optimal and used in most of the detailed simulations.

A view of the entire grid can be seen in Fig. 3.Here, the stator is shown in red, the rotor in green and the outflow part in blue. For clarity of the view, only few of the grid lines are shown. A detailed view of the leading edge of the rotor blade is displayed in Fig.4a and 4b. In the left part of Figure 4, the entire rotor is shown as seen looking in negative radial direction. Clearly visible is the step just ahead of the leading edge, making the generation of a proper grid at this location rather difficult. A more detailed view of this location is showing the structured grid, clearly demonstrating the high degree of resolution in this critical area. The grid, shown in Figures 3, 4a and 4b, had approximately 1,000,000 cells, covering all relevant boundary layers at the hub, the casing and the blades. The

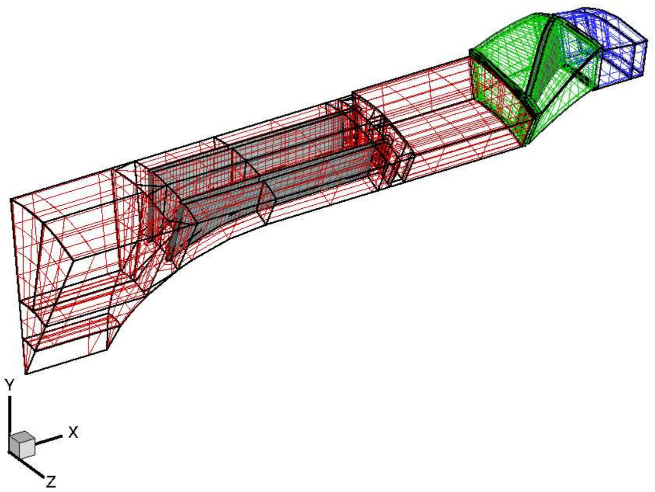

Figure 3: View of the entire computational grid.

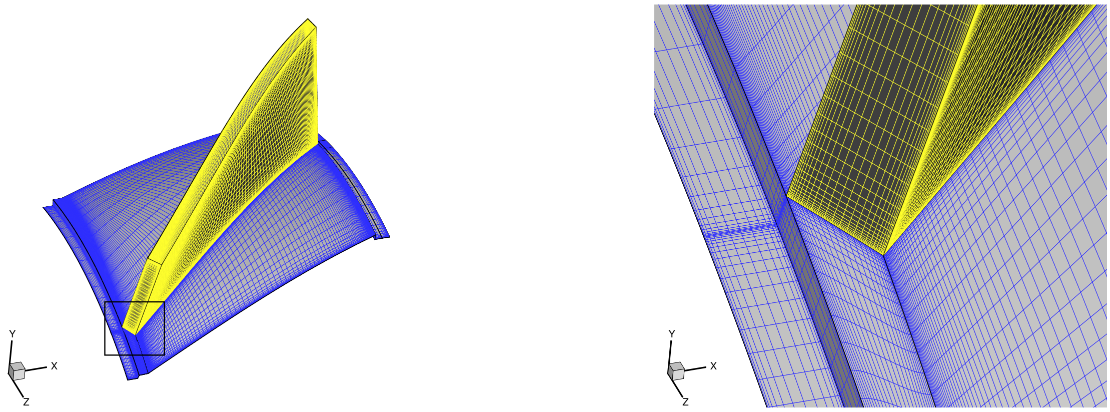

Figure 4: Surface grid on the rotor and the hub (left) and a detailed view of the structured grid at the rotor leading edge (right).

grid, consisting of 51 blocks, was mostly structured, with the only unstructured part at the centerline in front of the huband in the wake of the stator. The flow enters the meter axially in the positive x-direction (see Fig. 2 and 3). It passes at first the central body (hub) with the guide vanes of the first stator, entering then the rotor. The speed of rotation of the rotor is input, given by the experimental data available for the corresponding case. As explained above, only two passages of the stator and of the rotor were simulated, so that the boundaries between each segment could be treated as periodic. During the postprocessing, the results from one passage were used to reconstruct the flow field in the remaining passages by copying.

In the circumferential direction, 58 grid points resolved the blade to blade plane on the medium grid. An exponential distribution close to the wall provided very small distances of the first cells to the wall so that at least 16 points in direction normal to the wall were within the boundary layer. The distance of the center of the first cell from the nearest wall corresponded to y^+ between 0.5 and 1.0. This implied that in the Fluent computations, the k-ϵ turbulence model was mostly used without wall functions. In the radial direction, 52 grid points were distributed over the height of the blade with exponential distributions close to the walls. 20 grid points were positioned in the radial direction in the tip gap between the rotor blades and the outer casing.

Determination of the speed of rotation

During the initial phase of the present work it was found out that the flow in the rotor clearly indicated that there was a tangential force present, meaning that either the input rotational velocity or the throughflow were not correctly matched. This is possible, since the simulated flow meter is slightly different from the real one. The tangential force (lift on the baldes) resulted in a residual moment about the axis of rotation (x-axis). Clearly, the resulting flow field was not the actual one, as in reality the moment is very close to zero. The authors therefore decided to find a rotational speed that would match the given axial velocity (given by the required volumetric flow rate) and result in zero moment in the axial direction.

The rotational speed ω could be determined only iteratively. Before embarking on this endvor, one should realize that the procedure is very time consuming, since the resulting moment is first obtained by integration over the rotor blade surface and then has to be averaged over a time period that is much longer than the blade passing periodic time, $\Delta T \gg T$, where $T = \frac{1}{f}$ and f is the blade passing frequency.

As the simulation of three-dimensional, unsteady flows is very time consuming and requires large amounts of computer memory, the above iterative proccedure was carried out on the coarse grids only, with a subsequent simulation on the medium or fine grid. The influence of the local viscous effects was in this global consideration of secondary importance.

Assuming that the relationship between the mean coefficient of moment $\bar{c_m}$, obtained by averaging c_m in time, defined as:

$$c_m = \frac{M_{pr} + M_{visc}}{\frac{1}{2}\,\rho_{ref}\,c_{ref}^2\,A_{ref}} \tag{1}$$

was linear within a small region close to $\bar{c_m} = 0$, the rotational speed ω_{max} was perturbed by ±2%. In the above equation, M denotes moments due to viscous ($visc$) and pressure (pr) forces. The subscript ref denotes a reference state defined as the inflow conditions. A_{ref} is the area of the rotor blade calculated by the product of chord length and height of the blade.

The simualtion was run 10 blade passing periods, representing Δt, and then c_m was averaged over this time. The timewise history of the total moment coefficient c_m over one blade is given in Figure 5a (left) for the maximum volume flow rate Q_{max} for three different rotational speeds ω: reference value given by the experiments and the two rotational speeds deviated by ±2%. It is obvious that the timewise average value changes depending on the rotational speed. The simulated relationship of the resulting averaged coefficient of moment is shown in Figure 5b (right). As assumed, the relationship is nearly perfectly linear, making an interpolation to $\bar{c_m} = 0$ rather easy.

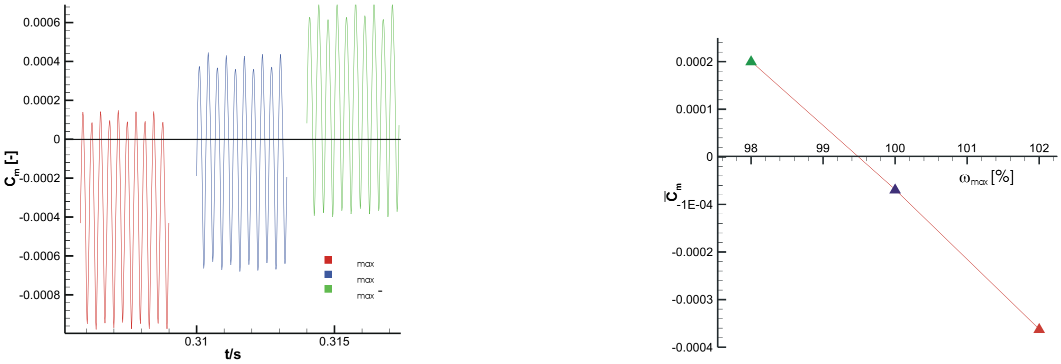

Figure 5: History of coefficient of moment c_m (left) and its mean value $\bar{c_m}$ as a function of ω (right) for Q_{max}.

It is interesting to note that in the case of Q_{max}, the numerically determined rotational speed for $\bar{c_m} = 0$ was approximately 0.5% below the value of ω_{max} given by the experiments.

Similarly, the correct operating speed of rotation was determined for the volume flow rate of $Q = 0.1 \cdot Q_{max}$. The corresponding histories of c_m are displayed in Fig. 6a (left), with the resulting relationship between the $\bar{c_m}$ and ω shown in Figure 6b (right). In this case, the numerical rotational speed was larger than the reference value obtained from experimental data, showing a difference of approximately 0.3%.

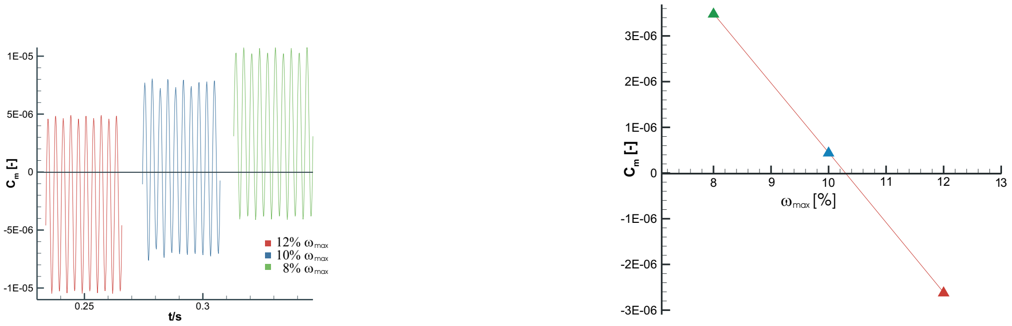

Figure 6: History of coefficient of moment c_m (left) and its mean value $\bar{c_m}$ as a function of ω (right) for $Q = 0.1 \cdot Q_{max}$.

Finaly, the result of the above iteration was verified by a computation on the finest grid. Table 1. summerizes the numerical results. For both volumetric flows the $\bar{c_m}$ could be reduced by two orders of magnitude.

Table 1: c_m coefficients before and after the correction.

vol. flow rate	original c_m	computed c_m
Q_{max}	$-6.87 \cdot 10^{-5}$	$-3.83 \cdot 10^{-7}$
$0.1 \cdot Q_{max}$	$4.49 \cdot 10^{-7}$	$3.1 \cdot 10^{-9}$

Results

The corrected operating conditions were used to simulate the two volume flow rates. The inflow conditions are summerized in Table 2. As pointed out above, the simulations were performed on the medium grid with 1 million grid cells, as this grid was considered to a reasonable compromise. The following discussion will concentrate on the flow details in various regions of the flow field for the case of Q_{max}.

Table 2: Summary of inflow parameters.

flow variable	Q_{max}	$0.1 \cdot Q_{max}$
flow rate	$250\ m^3/h$	$25\ m^3/h$
temperature	293.15	293.15
velocity	14.72 m/s	1.47 m/s
pressure	1 bar	1 bar
Re	$74 \cdot 10^3$	$7.4 \cdot 10^3$

The static gauge pressure relative to the inflow static pressureon is shown on the surface of the entire flow meter in Figure 7.
As the flow enters the guide vanes, the cross-sectional area is reduced by the central body, accelerating the flow as indicated by the decreasing pressure on the hub of the central body in Figure 7. A stagnation point develops at the front of the central body. The unsteady fluctuations of the static pressure on the walls indicate that there is some influence of the rotor on the flow in the guide vanes. The region of stagnation point changes in size periodically with the rotor passing the stator vanes. There was no evidence of flow separation on the hub, as the pressure uniformly decreases along its surface in the streamwise direction. A detailed view of the static pressure contours in the rotor is offered in Figure 8. An increasing stagnation pressure at the leading edge can be noticed, indicating radial increase of the relative velocity. The stagnation pressure decreases in the boundary layers.
The static pressure contours combined with the streamline at the rotor leading edge (left) and at the trailing edge (right) are displayed in Figure 9. Interesting is the small separation zone behind the sharp edges at the leading edge. At the blunt trailing edge, a massively separated region develops, leading to an unsteady wake.

The flow field in the rotor can be viewed in Figure 10. In the left part, three plane cuts numbered 1 - 3 are shown, with the corresponding contours of the magnitude of the absolute velocity. In all planes the influence of the boundary layers and, behind the trailing edge, wake can be recognized as a velocity deficit. In the right part of Figure 10, the three velocity components in the axial, radial and circumferential directions can be seen on plane 1. The wake as well as the secondary flow are clearly recognized. Also evident is the influence of the rotor, seen in the tangential velocity distribution.
The three velocity components in the other two planes are displayed in Figure 11 together with the corresponding streamlines. The secondary vortices on the hub are clearly visible.

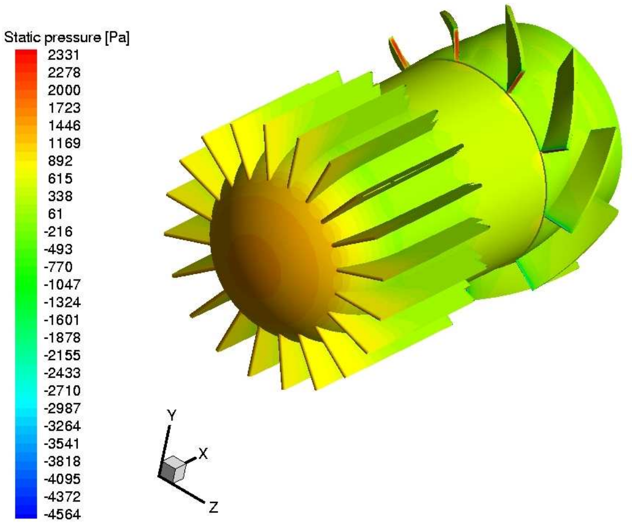

Figure 7: Static pressure contours on the walls of the flow meter.

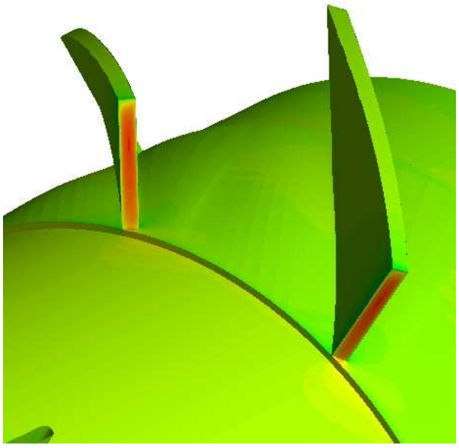

Figure 8: Static pressure contours in the rotor.

A similar view of the flow field in the rotor is given in Figure 12. The analysis of these results is made easier by using the relative point of view, meaning that the blade is stationary and the upper wall moves with negative velocity of approximately 45 m/s in the tangential direction.
There is significant flow through the tip gap, with a subsequent flow separation and wake on the lee side (pressure side). Strong secondary flow can bee seen on the suction side, with a distinct velocity defect at about 2/3 of the blade height. Again, the three velocity components are given in the right part of Figure 12. The relative velocities on the planes 2 and 3 are shown in Figure 13.
The tip gap flow is visible also in these two planes. In the picture of the axial velocity, the boundary layer thickness, seen as a location of minimum axial velocity, indicates that all the boundary layers were resolved adequately.

Conclusions

In the present study the flow field in the Elster TRZ DN80 turbine flow meter was investigated by three-dimensional numerical simulations for two different operating conditions. The simulations were carried out using the solver FLUENT version 6.x. The resulting 3-dimensional unsteady flow fields displayed many detailed features that made the explanation of several empirically observed phenomena possible. The flow in the tip gap was studied in some detail and recognized as mainly driven by viscous effects. The secondary flow was demonstrated and discussed.

Future work will concentrate on the geometric details of the rotor and stator regions in order to aid in the design process.

References

[1] R. C. Baker. Turbine Flowmeters: II. Theoretical and Experimental published Information. *Flow Measurement and Instrumentation*, 4(3):123–144, 1993.

[2] A. Brümmer. Der Einfluß von Druckpulsationen auf die Meßgenauigkeit von Turbinenradzählern. In *Workshop Kolbenverdichter*, Rheine, 29.-30.10. 1997.

[3] Fluent. Fluent 5, July 1998. Lebanon, NH, USA.

[4] D. J. Gestler. The Auto-Adjust Turbo-Meter and how it Developed. *Pipeline & Gas Journal*, July, 1980.

[5] Th. Hüwener, E. von Lavante, R. Ernst, and W. Schieber. Numerical Investigation of Flow Effects on Accuracy in Turbine Flow Meters. In *Proceedings of the 10th International Conference on Flow Measurement, FLOMEKO '2000*, page 41, Salvador, Brazil, June, 04-08, 2000.

[6] M. Kallenberg. Numerische Simulation der chemisch reagierenden Strö-mung in einer typischen Überschallbrennkammer. Dissertation. Universität GH Essen, 1999.

[7] P. M. A. van der Kam and K. van Dellen. The Effect of Double Bends out of Plane on Turbine Meters. *Flow Measurement Instrumentation*, 2:61–68, 1991.

[8] E. von Lavante, Th. Hüwener, R. Ernst, and W. Schieber. Numerical Investigation of the Flow Field in a 2-stage Turbine Flow Meter. In *Flow Measurement 2001*, Glasgow, Scotland, May, 08-10, 2001.

[9] W. F. Z. Lee. Performance of a Self-Adjusting Gas Turbine Meter. In *Proceedings of International Symposium on Fluid Flow Measurement*, AGA, November, 16-19, 1986.

[10] W. F. Z. Lee, D. C. Blakeslee, and R. V. White. A Self-Correcting and Self-Checking Gas Turbine Meter. *Journal of Fluids Engineering*, 104:143–149, 1982.

[11] W. F. Z. Lee and H. Karlby. A Study of Viscosity Effect and Its Compensation on Turbine-Type Flowmeters. *Journal of Basic Engineering, Transactions ASME*, 82:717–728, 1960.

[12] W. F. Z. Lee et al. *United States Patent, No. 4,305,281.* Rockwell International Corporation, 1981.

[13] N. Lehmann. Dynamisches Verhalten von Turbinenradgaszählern. *Das Gas- und Wasserfach*, 131(4):160–167, 1990.

[14] B. Mickan et al. Die Fehlerverschiebung eines Turbinenradgaszählers in Abhängigkeit vom Anströmprofil. *PTB-Mitteilungen*, 106(2):113–124, 1996.

[15] S. Perpeet. Numerische Simulation von Strömungsfeldern um Durchfluß-Meßanordnungen. Dissertation. Universität GH Essen, 2000.

[16] W. Schieber. A Turbine Meter with Built-in Transfer Prover. In *Proceedings of the 9th International Conference on Flow Measurement, FLOMEKO '98*, pages 509–516, Lund, Sweden, June, 15-17, 1998.

[17] W. Schieber. *Estimating Meter Error form Rotor Spin Time Test.* American Meter Company, 1999.

[18] J. Yao. Numerische Simulation der Multi-Dimensionalen Strömung in Kolbenmotoren. Dissertation. Universität GH Essen, 1997.

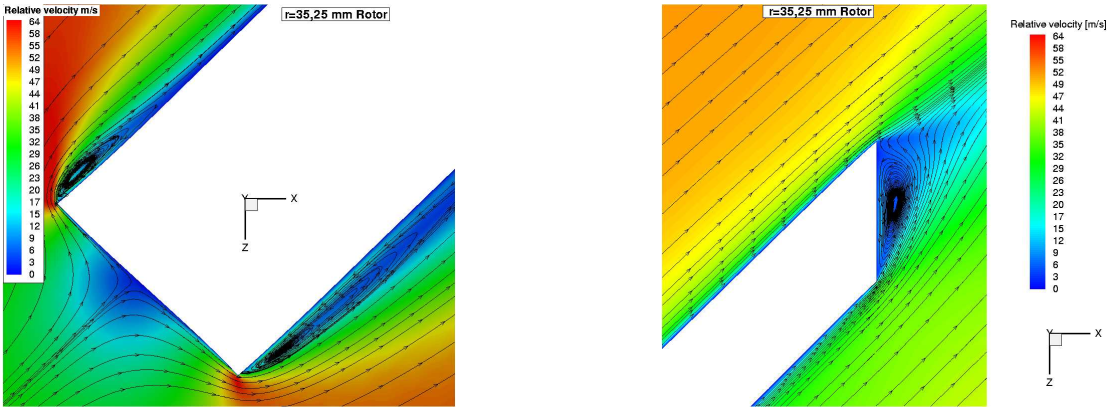

Figure 9: Static pressure and streamlines at the rotor leading edge (left) and trailing edge (right).

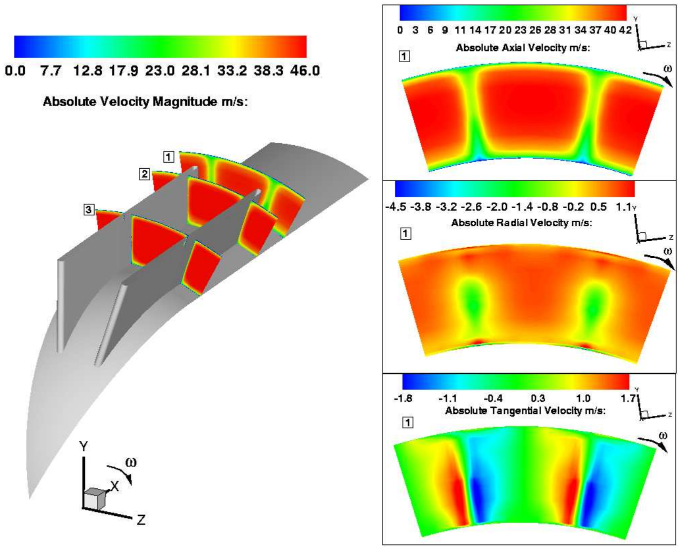

Figure 10: Absolute velocities in the stator.

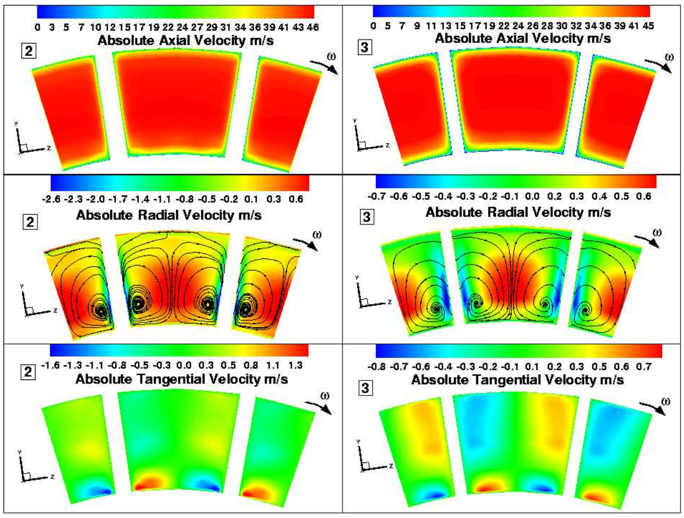

Figure 11: Absolute velocities in the stator.

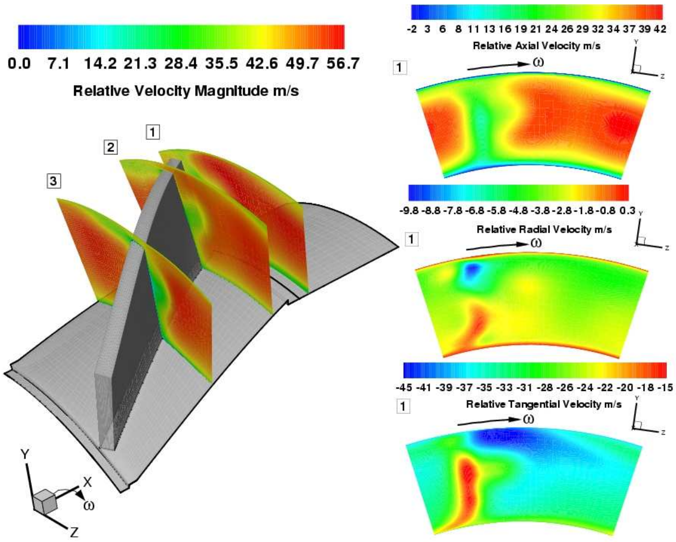

Figure 12: Relative velocities in the rotor.

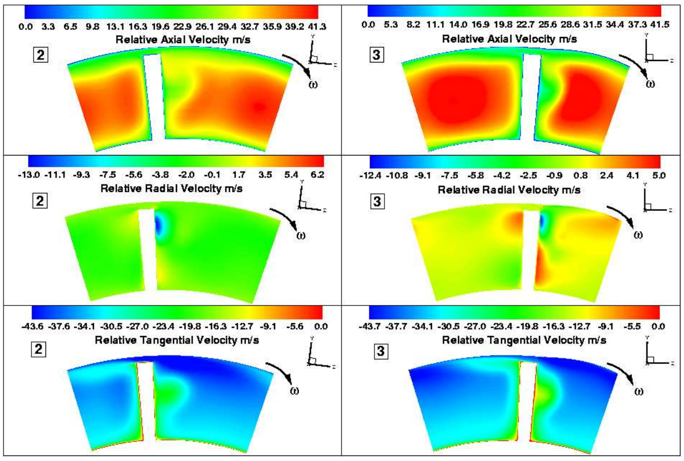

Figure 13: Relative velocities in the rotor.